Nano Convergence

REVIEW

Open Access

Rational design of photocatalysts for ammonia production from water and nitrogen gas

Seokwoo Choe[1], Sung Min Kim[1], Yeji Lee[1], Jin Seok[1], Jiyong Jung[1], Jae Sung Lee[2*] and Youn Jeong Jang[1*]

Abstract

Photocatalytic N_2 reduction has emerged as one of the most attractive routes to produce NH_3 as a useful commodity for chemicals used in industries and as a carbon-free energy source. Recently, significant progress has been made in understanding, exploring, and designing efficient photocatalyst. In this review, we outline the important mechanistic and experimental procedures for photocatalytic NH_3 production. In addition, we review effective strategies on development of photocatalysts. Finally, our analyses on the characteristics and modifications of photocatalysts have been summarized, based on which we discuss the possible future research directions, particularly on preparing more efficient catalysts. Overall, this review provides insights on improving photocatalytic NH_3 production and designing solar-driven chemical conversions.

Keywords: Photocatalyst, Ammonia, Nitrogen

1 Introduction

Recently, there has been an increasing focus on ammonia (NH_3) as not only a key commodity for chemicals widely used in industries [1, 2], but also as a liquid energy carrier [3] that enables transport and supply of hydrogen (H_2) gas through cracking. Furthermore, NH_3 is an alternative carbon-free energy source that can be utilized in energy-conversion devices, for example, direct NH_3 fuel cells [4, 5]. Traditionally, NH_3 production has mainly relied on the Haber–Bosch process, which is energy intensive and generates considerable volume of CO_2 into the atmosphere because of these requirements, along with the needs for H_2 and the extreme operation condition [6].

Photochemical NH_3 production using N_2 and water as a hydrogen source at ambient temperature and pressure can offer a promising alternative route that is less energy intensive and reduces CO_2 emission, thereby significantly reducing environmental concerns [7]. NH_3 production paired with water oxidation is a thermodynamically uphill reaction; therefore, external energy input is necessary [8]. Photocatalysts can utilize solar energy, which is supplied to Earth with sufficient solar power and abundance and facilitate NH_3 production. Since TiO_2 photocatalysts applied to N_2 reduction, new photocatalysts and their modifications have been intensively suggested to improve photocatalytic NH_3 production [9].

Major advances in metal oxides such as TiO_2, WO_3, and $SrTiO_3$, bismuth oxyhalides, and polymeric carbon nitride photocatalysts have resulted in interests in the development of photocatalysts and their applications for NH_3 production [10–14]. This review is composed of mainly two sections: (1) fundamentals for photocatalytic NH_3 production, (2) strategies to develop photocatalysts. The first section focuses on the principles and mechanisms involved in the overall photocatalytic reaction. The second section contains recent progresses in the development of catalysts and their major advantages with regard to catalytic performance. The insights and discussions

*Correspondence: jlee1234@unist.ac.kr; yjjang53@hanyang.ac.kr
[1] Department of Chemical Engineering, Hanyang University, 222 Wangsimni-ro, Seongdong-gu, Seoul 04763, Republic of Korea
[2] Department of Energy and Chemical Engineering, Ulsan National Institute and Science and Technology, 50, UNIST-gil, Ulsan 44919, Republic of Korea
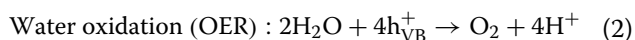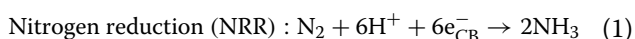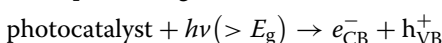
Springer Open

provided in this review will serve as useful resources for further development of photocatalysts and provide future research direction for photocatalytic NH_3 production.

2 Fundamentals for photocatalytic NH_3 production

2.1 Principle and mechanism

NH_3 production by N_2 reduction $(N_2(g) + 6H^+ + 6e^- \rightleftharpoons 2NH_3(g)$, $E^0 = 0.092$ V vs. SHE) paired with O_2 production by water oxidation $(2H_2O(l) \rightleftharpoons O_2(g) + 4H^+ + 4e^-$, $E^0 = 1.229$ V vs. SHE) is a thermodynamically uphill reaction that requires a potential of at least 1.137 eV [15] per electron [16]. Moreover, three electrons are required to produce an NH_3 molecule, and four holes are required to produce an O_2 molecule according to eqns. (1) and (2):

$$\text{Absorption of light}:$$
$$\text{photocatalyst} + h\nu\left(> E_g\right) \rightarrow e^-_{CB} + h^+_{VB}$$

$$\text{Nitrogen reduction (NRR)}: N_2 + 6H^+ + 6e^-_{CB} \rightarrow 2NH_3 \quad (1)$$

$$\text{Water oxidation (OER)}: 2H_2O + 4h^+_{VB} \rightarrow O_2 + 4H^+ \quad (2)$$

A simplified schematic diagram for photocatalyic NH_3 production and challenges in designing photocatalysts are summarized in Fig. 1. For overall NH_3 production, photons with energies > 1.137 eV are required to generate photoexcited electron–hole pairs that carry out the desired redox reactions at the active sites on the surfaces of the photocatalysts. Thus, a photocatalyst must have an energy band gap, $(E_g = E_{CBM} - E_{VBM}$, where CBM and VBM represent conduction band minimum and valence band maximum), larger than the energy required for the overall NH_3 production. In addition, a photocatalyst must have a suitable conduction and valence band alignment to drive two half-reactions using photoexcited electrons (e^-) and holes (h^+) under solar light irradiation.

The major factors to consider for photocatalyst designs are (1) photon absorption followed by photoexcited carrier generation, (2) their migration and separation, and (3) their consumption by redox reactions on the surfaces of photocatalysts. The dominant photon energy spectrum obtained from the sunlight is in the range of 390–700 nm. Furthermore, because photocatalytic redox reactions require kinetic overpotentials, photocatalysts have a bandgap energy in the range of 1.6–2.4 eV. The generated photoexcited carriers can migrate to active sites on the surface where redox reactions carried out. However, since the kinetics of carrier recombination in the interiors of the photocatalysts is fast, considerable amounts of photoexcited carriers are recombined [17]. Moreover, photoexcited carriers can be trapped in the interior and surface of the photocatalyst, which causes photocorrosion. Thus, a photocatalyst design to improve electron–hole pair migration and separation is important for further development of photochemical NH_3 production [18].

Most semiconductors that act as light absorbers in photocatalysts are inactive in the redox reactions with the photoexcited carriers; thus, the active sites on the surface of semiconductor are decorated with cocatalysts [19]. For example, cocatalysts, such as RuO_x, CoO_x, and Co-pi [20–22], combined on the surface of the semiconductor for facile water oxidation by providing active sites. Another critical point to note in NH_3 production via photochemical N_2 reduction is the facile competitive hydrogen evolution reaction by water reduction. NH_3 production is kinetically much more complex than water reduction, although the thermodynamic requirements for those reactions are similar [23]. This indicates that photochemical H_2 production may be predominant, resulting in inactive NH_3 production. Thus, it is critical to modify the surface that provides active sites for the desired redox reaction using suppressing competitive reactions on the semiconductors.

It is also necessary to note the importance of rate balance for photocatalytic reactions on photocatalysts. Since electrons and holes are generated in pairs under illuminations, their consumption must be coupled as well. For instance, if oxidation reactions involving photogenerated holes are sluggish, the total NH_3 production rate should be similar. In this case, scavengers, such as ethanol, methanol, and sulfites, can be employed as sacrificial reagents to facilitate oxidation reaction using photoexcited holes, thereby preventing from photoexcited carrier recombination [24]. However, since scavengers may interfere with counter reactions, here N_2 reduction, or product evaluation methods, the target scavenger should be chosen carefully. It is discussed in detail in the next section.

2.2 Experimental process

The simplest photocatalytic NH_3 production set-up is a particulate PC system where photocatalysts are dispersed in a medium, typically pure water, with N_2 bubbling under simulated solar light illumination, as shown in Fig. 1b. NH_3 and O_2 are generated on a single photocatalyst. The produced NH_3 is technically evaluated by the spectrophotometric method via the indophenol blue method or quantified using proton nuclear magnetic resonance spectroscopy (^{1}H-NMR) with isotope labeled nitrogen ^{15}N as shown in Fig. 2.

The indophenol blue method is based on the principle of the Berthelot reaction, where typically, salicylic acid, citrate, hypochlorite, and ferricyanide are used in

Choe *et al. Nano Convergence* (2021) 8:22

Page 3 of 12
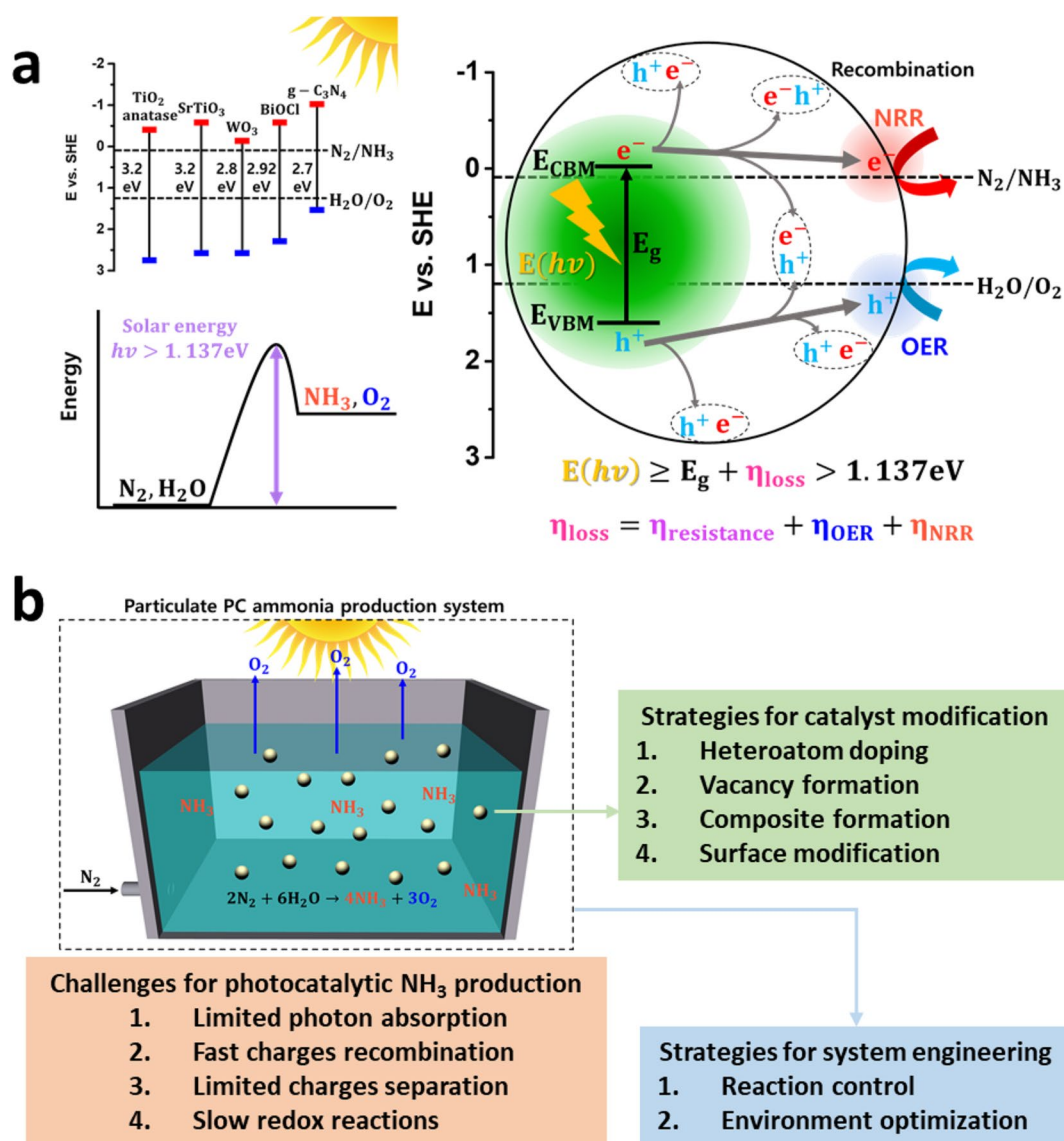
Fig. 1 a The schematic illustration of photochemical nitrogen reduction reaction [15]. **b** The challenges and strategies for photocatalytic NH_3 production in particulate photocatalytic (PC) ammonia production system

an alkaline solution. In the presence of NH_4^+, the color of the yellowish indicating solution, which contains the reagents, turns to blue, corresponding to 655 nm. As shown in Fig. 2a and b, thus, the concentration of NH_3 can be quantified by measuring the absorbance change at 655 nm using a UV–Vis spectrophotometer [28]. However, to quantify the concentration of NH_3 generated by photocatalytic N_2 reduction, multiple possible contaminants that interfere with the evaluation should be fully controlled [28]. For example, methanol, a widely used as a hole scavenger, and its derivatives cause incorrect color changes and significantly decrease the accuracy of NH_3

quantification as shown in Fig. 2c and d. Another critical point for NH_3, which is photocatalytically produced, quantification is to eliminate the parts from NH_3 contaminants, unintentionally present introduced through catalyst, components in set-up [26] or even the air. In fact, NH_3 present in human breath, sanitizers, and so can rapidly accumulate in water [29].

The most rigorous procedure to quantify photocatalytically generated NH_3 from N_2 reduction is to use isotope labeled $^{15}N_2$ gas. The photocatalytic reactions are conducted in a simple particulate system with $^{15}N_2$

Choe *et al. Nano Convergence*   (2021) 8:22

Page 4 of 12
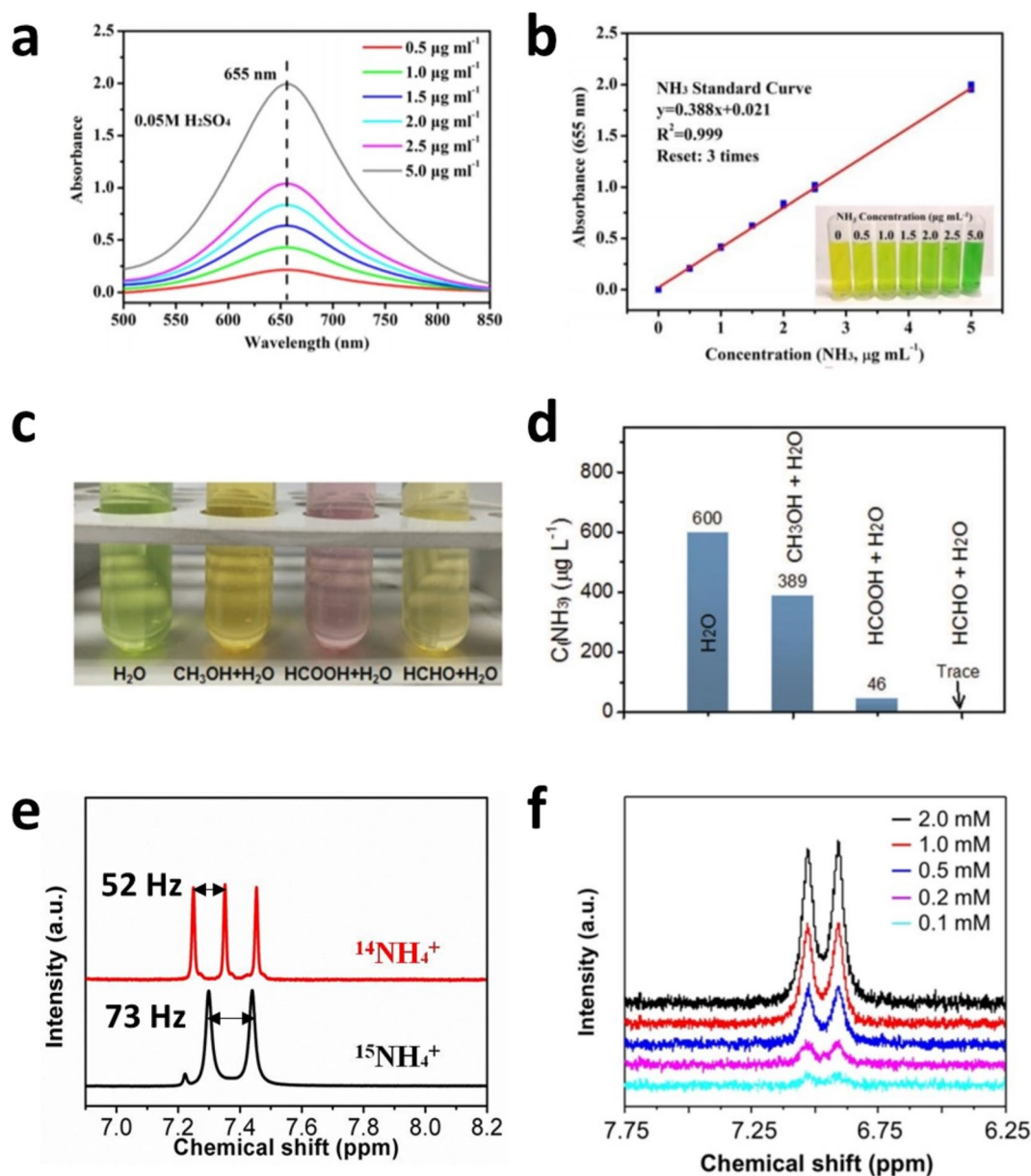
Fig. 2 **a** Spectrum and **b** standard curve of UV–Vis spectrophotometer with standard solutions from 0.5 to 5.0 μg·mL^{-1} in 0.05 M H$_2$SO$_4$. Reproduced with permission [25]. Copyright 2019, PNAS. **c**, **d** Interference impact on measurements of produced NH$_3$ in solution with CH$_3$OH, HCOOH and HCHO. Reproduced with permission [26]. Copyright 2019, Wiley–VCH. **e** ^{1}H-NMR spectrums of ^{14}NH$_4$$^+$(red) and ^{15}NH$_4$$^+$(black), respectively. Reproduced with permission [27]. Copyright 2021, The Royal Society of Chemistry. **f** The peaks for ^{14}NH$_4$$^+$ corresponding to its concentration. Reproduced with permission [8]. Copyright 2020, American Chemical Society

bubbling. Since the splitting of ^{1}H resonance in ^{15}NH$_4$$^+$ and ^{14}NH$_4$$^+$ resulting from the difference in the scalar interaction between N (^{15}N or ^{14}N) and H is differentiated, the ^{15}NH$_4$$^+$ produced, which is dissolved in an aqueous reacting solution, can be quantified by ^{1}H-NMR [30]. For instance, the ^{1}H resonance in ^{15}NH$_4$$^+$ can be split into two symmetric signals with a spacing of 73 Hz, whereas the resonance in ^{14}NH$_4$$^+$ can be split into three

symmetric signals with a spacing of 52 Hz as shown in Fig. 2e. Thus, false positive evaluations for the produced NH$_3$ can be prevented effectively.

3 Strategies to develop photocatalysts

This section is divided into mainly two parts: (1) semiconductors comprising photocatalysts, which have been widely applied as a light absorber in Fig. 3a, and (2)

Choe *et al. Nano Convergence* (2021) 8:22

Page 5 of 12
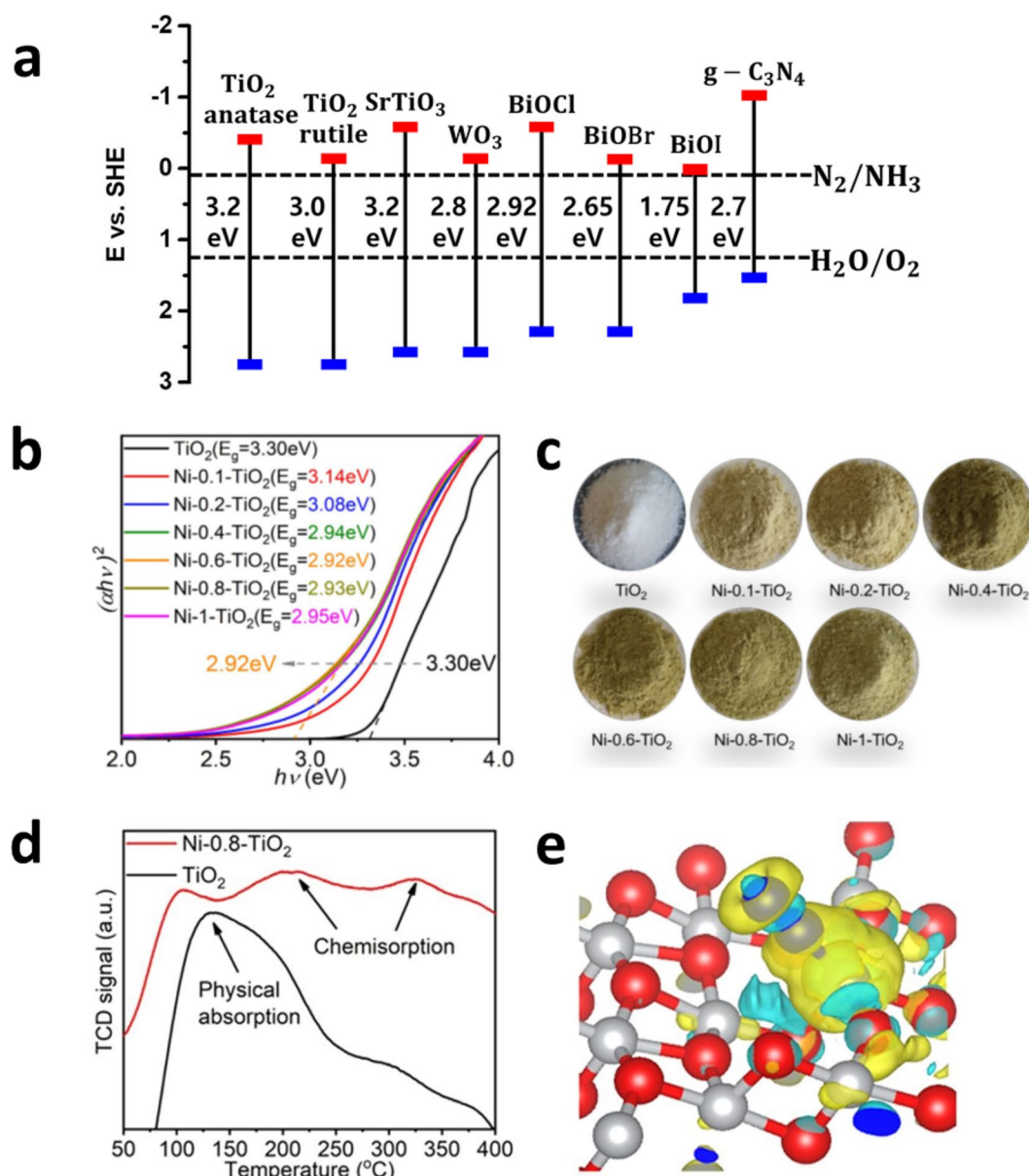
Fig. 3 a The band alignments of widely used photocatalysts. **b** The Tauc plot $(ahv)^2$ versus (hv) for the caluate the optical band gap energy E_g. **c** The color of Ni-x-TiO$_2$ gradually deepens with the increase of the amount of Ni^{2+}. **d** The N$_2$-TCD spectrums of Ni-0.8-TiO$_2$(red) and TiO$_2$(black), respectively. **e** Bader charge density difference of Ni doped TiO$_2$; Ti(silver), Ni(blue), and O(red). Reproduced with permission [45]. Copyright 2020, Americal Chemical Society

strategies to modify the catalysts, which have been effectively used to further increase the photocatalytic NH$_3$ production.

3.1 Semiconductors
Titanium(Ti)-based oxides Titanium dioxide, TiO$_2$, possesses several advantages that make it attractive for use in photocatalytic NH$_3$ production. TiO$_2$ has a bandgap of ~3.2 eV, which absorbs UV light, and a CBM and

VBM that offer sufficient overpotential for the photoexcited electrons to reduce N$_2$ to NH$_3$ and holes to oxidize water to O$_2$, respectively. In addition, the inexpensive, environmentally benign, and stable nature of TiO$_2$ is an additional advantage. Historically, the primary limitation of using TiO$_2$ has been rapid photoexcited electron–hole recombination, which is similar to many other oxide-based photocatalysts. Strontium titanate, SrTiO$_3$ [31], is another candidate showing two major benefits over

Choe *et al. Nano Convergence*   (2021) 8:22

Page 6 of 12

TiO_2 for use in the NH_3 production. The CBM of $SrTiO_3$ is slightly more negative than that of TiO_2, thereby providing a stronger driving force to reduce N_2 using the photoexcited electrons. In addition, intrinsic charge mobility in $SrTiO_3$ is higher than that in TiO_2, thereby suppressing photoexcited charge recombination [32]. However, despite this thermodynamic advantage, the photocatalytic NH_3 production using TiO_2 or $SrTiO_3$ is limited because of ineffective light absorption resulting from their wide bandgaps and inactive redox reactions due to the limited active sites on their surface. Recently, many attempts have been made to address these limitations, which include doping, coupling with electrocatalysts (cocatalysts), surface defect engineering, and so on [33–35].

Bismuth oxyhalide (BiOX) BiOX (X = Cl, Br, and I) has a layered structure where bismuth and oxygen layers (BiOx) are connected with halide (X) layers alternatingly via Van der Waals forces [36]. Since the VBM is determined by O 2p and X δ p (δ = 3, 4, and 5, corresponding to X = Cl, Br, and I, respectively) and the CBM is mainly evaluated by Bi 6p, their band alignments and bandgap are varied depending on the element comprising the semiconductors [37]. For example, BiOCl, BiOBr, and BiOI have bandgap energies of 2.92, 2.65, and 1.75 eV, respectively [38], and are thermodynamically suitable for NH_3 production, they enable the production of NH_3 and O_2 by the overall photocatalytic N_2 reduction. However, despite these advantages, BiOX semiconductors have severe drawbacks when using them as photocatalysts, mainly due to the insufficient photogenerated charge separation in the bulk and surface. Recently, their fundamental limitations have been investigated, and strategies to improve their photocatalytic performances have been explored.

Graphitic carbon nitride (g-C_3N_4) g-C_3N_4 is a polymeric semiconductor with a bandgap energy of 2.7 eV and appropriate positions for the CBM and VBM for the NH_3 and O_2 production, respectively [39]. However, since rapid photoexcited carrier recombination in the bulk results in limited charge separation in the redox reactions and ineffective N_2 adsorption on the surface, as an initial step for N_2 reduction, multiple advancements to develop g-C_3N_4 have been suggested [40].

3.2 Strategies to enhance photocatalytic NH_3 production
As described in the introduction section, photocatalysts comprising semiconductors can produce NH_3 using N_2 and water under illumination. However, the typical NH_3 production rate and efficiency of intrinsic semiconductors using solar energy have been far lower than those

expected from their bandgap energies. The major limiting factors include (1) limited light absorption because of the intrinsically large bandgaps, (2) significantly fast photoexcited electron–hole pairs recombination, and (3) slow redox reactions including N_2 reduction and water oxidation. Recently, many strategies have been made to address one or more of these challenges, which include engineering defects by extrinsic doping or vacancy introducing, composites forming using multi-light absorbers, and coupling with electrocatalysts. This section will give an overview of each of these attempts and discuss how these strategies affected the photocatalytic NH_3 production.

3.2.1 Defect engineering
Defect engineering has been widely suggested to control bulk and surface properties of catalysts, for example, by heteroatoms doping, vacancies formation, and so on. This defect engineering enhances photocatalytic NH_3 production by changing the light absorption properties, improving charge separation efficiencies, or facilitating surface redox reactions, and it generally influences the multi-mechanistic steps of light harvesting simultaneously [41].

Heteroatom doping Heteroatom doping involves intentional introduction of impurity atoms into the lattices of materials to change their optical and electrical properties [42–44]. Depending on the species and degree (concentration) of dopants, changes, in the bandgap energy, band alignment, charge separation efficiency, and N_2 adsorption ability are expected. However, since dopants can provide electron–hole recombination sites or prohibit charge transports, identifying types and concentrations of dopants appropriate for the photocatalytic process is important.

Zaicheng Sun and coworkers prepared a nickel-doped TiO_2 (Ni-x-TiO_2, where x = concentration of the Ni precursor controlled in the preparation step) photocatalyst using the sol–gel method [45] show Their optimized sample (Ni-0.8-TiO_2) exhibited an NH_3 production rate of 46.80 $\mu mol \cdot g^{-1} \cdot h^{-1}$ under simulated solar light irradiation, which is seven times higher than the rate using pure reference TiO_2. The Ni-0.8-TiO_2 sample extends the light absorption range to the visible light region with a bandgap energy of 2.92 eV, whereas pure TiO_2 absorbs only UV light with a bandgap energy of 3.2 eV as shown in Fig. 3b. As Ni atoms having 2 + valence that replace the Ti site having 4 + valence, oxygen vacancies (Ov) are created naturally for charge neutrality within the host semiconductors, and they vary the band position of the CBM and VBM in TiO_2, which results in a decrease in the bandgap energy. Besides changes in the optical properties, N_2

adsorption, the initiation step for NH_3 production from N_2, is enhanced by Ni doping on TiO_2, as investigated using a N_2 temperature programmed desorption spectroscopy (N_2-TPD) and a computational analysis.

Tierui Zhang and coworkers prepared a copper-doped TiO_2 nanosheet (x%-TiO_2, where x = molar ration of Cu/Ti controlled in the preparation step) photocatalyst using a hydrothermal method [46]. The optimized sample, 6%-TiO_2, exhibited an NH_3 production rate of 78.9 $\mu mol \cdot g^{-1} \cdot h^{-1}$, whereas pristine TiO_2 nanosheets exhibited a rate of 0.34 $\mu mol \cdot g^{-1} \cdot h^{-1}$. As Cu heteroatoms replaced the sites of Ti in the TiO_2 nanosheets, small amounts of Ti^{3+} valence states in Ti^{4+}-dominant TiO_2 and Ov sites are created, as observed using X-ray photoelectron spectroscopy and X-ray absorption fine structure spectroscopy. Furthermore, owing to the difference in size between the Cu^{2+} dopants and Ti^{4+} hosts, Cu-doped TiO_2 has a compressive strain, which is evaluated by DFT calculations, and it causes changes in the distribution in the electron densities around O and Ti in the materials. The combination of non-stoichiometry and lattice strain in Cu-doped TiO_2 narrows its bandgap energy, corresponding to the extended light absorption range of 600–800 nm, and electrons are accumulated around the sites of O atoms, thereby affecting the changes in the N_2 adsorption affinity.

Jing Zhang and coworkers prepared a Fe-doped $SrTiO_3$ ($Fe_xSr_{1-x}TiO_3$, where x = the stoichiometric ratio of Fe precursor and Sr precursor controlled in preparation step) photocatalyst using the hydrothermal method followed by calcination [47]. The $Fe_{0.1}Sr_{0.9}TiO_3$ sample exhibited the best NH_3 production rate of 30.1 $\mu mol \cdot g^{-1} \cdot h^{-1}$, which is 3.2 times higher than that of pristine $SrTiO_3$. By replacement of the Fe^{3+} ion, which has a smaller size, on the Sr^{2+} site in $SrTiO_3$, the size of particles is reduced along with the corresponding increase in the surface area. Furthermore, the $Fe_{0.1}Sr_{0.9}TiO_3$ photocatalyst exhibits significantly enhanced N_2 chemisorption and activation ability, which Fe dopants are the major contributor to.

Vacancies Vacancy, one of defect formation strategies, leads to changes in the band structure and chemical adsorption nature on the surface [48]. This section gives an overview of intentionally induced anion vacancies in semiconductor photocatalysts and discusses how they affected the photocatalytic NH_3 production.

Zhong Jin and coworkers compared the NH_3 production activities using BiOBr semiconductors in the presence (Vo–BiOBr) or absence (BiOBr) of oxygen vacancies [49]. The Vo-BiOBr samples were prepared using the hydrothermal method with the addition of polyvinylpyrrolidone surfactants leading to in-situ generation of abundant vacancies, whereas pristine BiOBrs were synthesized without adding the surfactants. The Vo-BiOBr photocatalysts produced NH_3 at a rate of 54.70 $\mu mol \cdot g^{-1} \cdot h^{-1}$ under UV–Vis irradiation, which is 10 times higher than the production rate using BiOBr. The major contribution of this significant improvement is enhanced N_2 adsorption that initiates the intermediate formation for NH_3 production. For example, the amount of adsorbed N_2, estimated based on N_2 adsorption isotherms, on Vo-BiOBr is considerably higher than that using BiOBr as shown in Fig. 4a. Furthermore, by introduction of the oxygen vacancies, the bandgap energy is reduced with the shifts in the CBM and VBM positions, which leads to increased light absorption as shown in Fig. 4b.

Chuanyi Wang and coworkers prepared metal-free g-C_3N_4 semiconductors by thermal decomposition of melamine and induced nitrogen vacancies (V-g-C_3N_4) within the semiconductors by additional calcination under a N_2 atmosphere [50]. The V-g-C_3N_4 samples produced NH_3 at a rate of 1240 $\mu mol \cdot g^{-1}$ h^{-1} using pure N_2 and water under visible light irradiation, whereas pristine g-C_3N_4 produced negligible amounts of NH_3. Further, morphologies and bandgap energies were not significantly varied depending on the intentional creation of N vacancies; however, two factors changed considerably. Due to the presence of N vacancies on the semiconductor, the signal collected using photoluminescence spectra decreased, indicating the reduction in the carrier recombination and enhancement of their separation. Furthermore, the N vacancies enable selective adsorption and activate N_2, and it was experimentally confirmed that negligible amount of NH_3 produced on g-C_3N_4 selectively blocked the vacancies using Pd particles.

3.2.2 Coupling with multi-light absorbers
Coupling with multi-light absorbers to form heterojunctions has been widely investigated to improve light absorption capacity under single illumination and separation of photoexcited electron–hole carriers through their designed band alignments. This strategy for catalyst design is effective in improving the photocatalytic NH_3 production.

Zhong Jin and coworkers prepared Bi_2MoO_6/Ov-BiOBr composites, where Ov denotes the oxygen vacancies using two-step methods, and synthesized Bi_2MoO_6 by solution-phase reflux process followed by the hydrothermal process to couple Ov-BiOBr on as-prepared Bi_2MoO_6 [51]. Despite minimal difference in light absorption before and after coupling, the Bi_2MoO_6/Ov-BiOBr composites showed a significantly enhanced NH_3
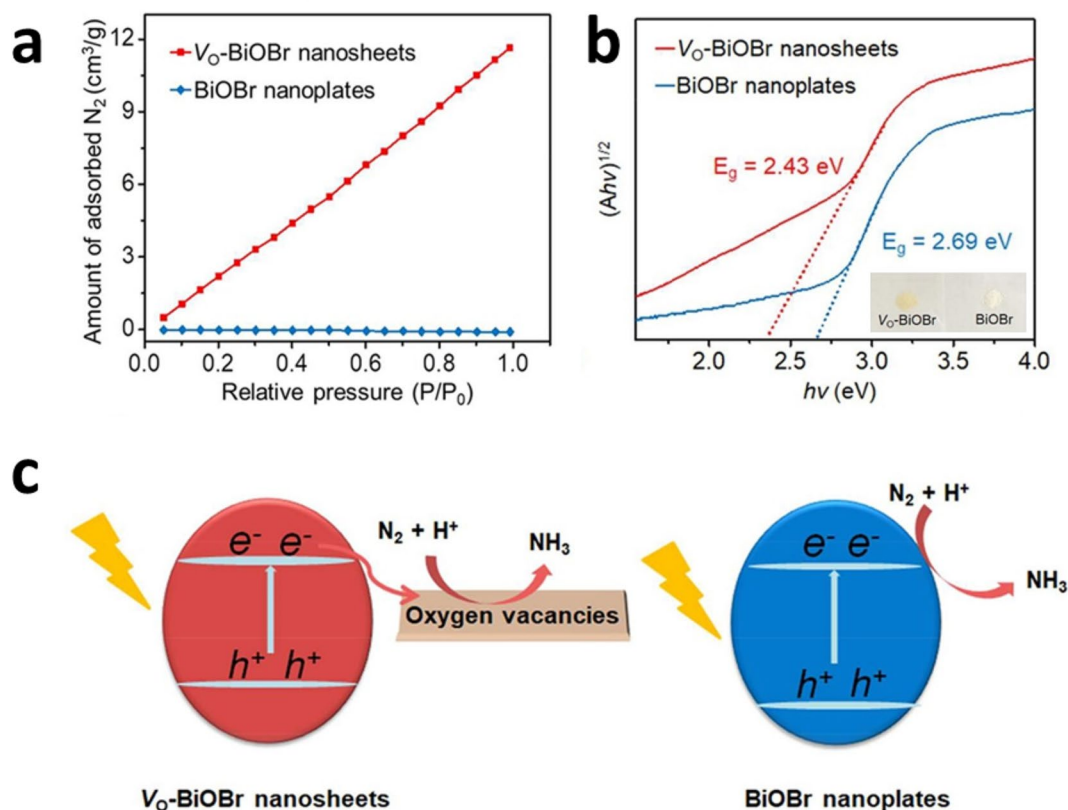
Fig. 4 **a** The N_2 adsorption isotherms, **b** The Tauc plot $(ahv)^2$ versus (hv) and **c** The schematic illustration of pohtocatalytic NH_3 synthesis process on Vo-BiOBr nanosheets and BiOBr nanoplates, respectively. Reproduced with permission [49]. Copyright 2018, American Chemical Society

production rate (90.7 μmol·g^{-1} h^{-1}), which is almost 30 and 3 times higher than the rates evaluated using Bi_2MoO_6 and Ov-BiOBr, respectively as shown in Fig. 5a. The major role of coupling is the formation of cascaded band alignments at the interface between two semiconductors. The photoexcited holes are transported and oxidize the electron donor on Bi_2MoO_6 where the VBM is located relatively higher, whereas the photoexcited electrons are transported and reduce N_2 on Ov-BiOBr where the CBM located relatively lower. Furthermore, oxygen vacancies on BiOBr show synergistic effects on the NH_3 production by providing N_2 adsorption and activation sites as shown in Fig. 5b.

Jimmy Yu and coworkers prepared Ov-TiO_2 using the hydrothermal method followed by loading Au nanoparticles. The Au nanoparticles generate hot electrons under visible light illumination [51], which is known as plasmonic phenomena. The hot electrons are injected into the CBM of TiO_2 and then trapped in vacant sites where N_2 is reduced into NH_3. The generated holes remain on Au and oxidize the electron donors, methanol, in solution as shown in Fig. 5c and d. The optimized Au/TiO_2-Ov samples produced NH_3 with a rate of 78.6 μmol·g^{-1}·h^{-1}

under visible light irradiation, which is at least 98 and 35 times higher those using Au/TiO_2 and TiO_2-Ov photocatalysts, respectively.

3.2.3 Surface modification and reaction engineering

As discussed above, photocatalytic activities have been developed significantly by modifying photocatalysts, for example, defects engineering and composite formation. However, although photogenerated charge generation and separation are advanced by multiple possible strategies, if the surfaces of the semiconductors exhibit slow charge injection and are poorly catalytic for N_2 reduction, the NH_3 production rate may not be enhanced directly. The surface modification on the semiconductors using a robust electrocatalyst (cocatalyst) for N_2 to NH_3 conversion is the simplest way to improve the limiting factor at the interface between the semiconductors and liquid where reactants are present. Therefore, the modification of the semiconductor surface with various NH_3 production catalysts, such as Ru, Cu, and Au, has been investigated [20, 34, 53].
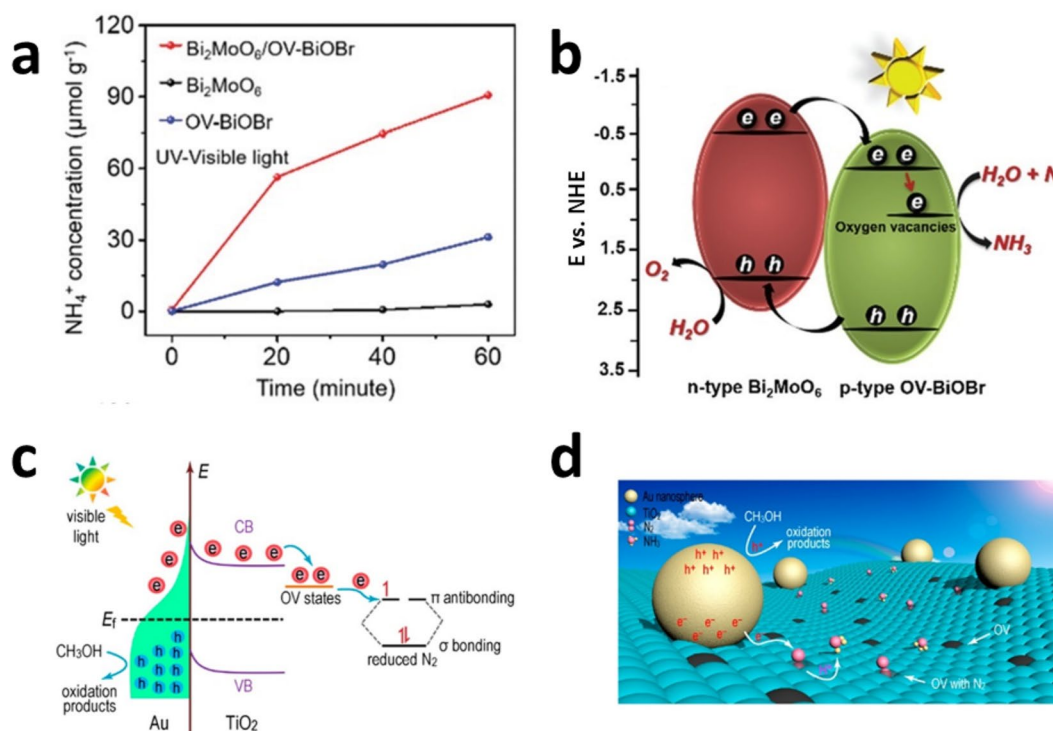
Fig. 5 **a** NH_4^+ concentrations of Bi_2MoO_6/Ov-BiOBr heterojunctions, Bi_2MoO_6 and BiOBr alone, respectively. **b** The scheme of proposed Bi_2MoO_6/BiOBr heterojunctions. Reproduced with permission [51]. Copyright 2019, The Royal Society of Chemistry. **c** The schematic reaction mechanism and **d** the artistic illustration of Au/TiO_2-Ov photocatalyst. Reproduced with permission [52]. Copyright 2018, American Chemical Society

In contrast, since the rates of reduction and oxidation reactions always correspond to one another, the sluggish photo-oxidation using holes may become a limiting factor for the photocatalytic NH_3 production. To overcome the possible limitation, it has been widely suggested to load appropriate electrocatalysts (cocatalysts) for water oxidation on the semiconductor or provide a more facile hole acceptor (electron donors) than water, such as methanol or ethanol (Table 1).

4 Summary and outlook

In summary, we reviewed the mechanistic and experimental steps for photocatalytic NH_3 production and examined various strategies to modify photocatalysts employed to enhance the production activities. This review clearly shows that although significant development of photocatalyts has been reported thus far, further advances for practical NH_3 production are required. First, the efficiency for charge generation via solar light absorption should be enhanced. Considering that the majority of incident photons are in the range of visible light, development of absorbers, can harvest the incident solar light, is required by determining appropriate materials and engineering semiconductors.

The charge separation effect is also required for photocatalytic NH_3 production through suppression of their recombination. For example, strategies for doping and composite formation will exhibit advances in the future and may increase the photon absorption efficiency simultaneously. In addition, morphology engineering [72–76] for photocatalysts will be promising and can be achieved by controlling the distances for carrier transportation and lifetime duration between the photo-induced generation and recombination. Furthermore, this may change facets and surface area, thereby providing active sites for the redox reactions using transported carriers. Moreover, if the facets are optimized with increasing surface area, morphology engineering can be significantly beneficial for NH_3 production.

With improvements in photon absorption and charge separation, surface engineering will be able to provide active sites where N_2 reduction using electrons and oxidation using holes is important. Thus, defect engineering, for example, formation of vacancies, cocatalyst coupling, and applying sacrificial reagents have been suggested. It is noteworthy that N_2 diffusivity control close to photocatalysts make an important contribution to practical photocatalytic NH_3 production. For instance,

Table 1 The summary of photocatalytic nitrogen reduction performances and its operating conditions: photocatalysts

Photocatalysts	Light source	Hole scavenger	Ammonia production rate	Ammonia detection methods	Refs
PCN/rGO(0.2)	250 W Xe lamp 400 nm < λ < 800 nm	1 mM EDTA-2Na	544.6 $\mu mol \cdot L^{-1} \cdot g^{-1} \cdot h^{-1}$	Nessler's reagent[b]	[14]
Ru/TiO$_2$	300 W Xe lamp	20% C_2H_5OH	3.31 $\mu mol \cdot g^{-1} \cdot h^{-1}$	Indophenol blue	[20]
Cu/g-C$_3$N$_4$	300 W Xe lamp 400 nm < λ < 800 nm	20% C_2H_5OH	186 $\mu mol \cdot g^{-1} \cdot h^{-1}$	Nessler's reagent	[34]
Ni-0.8-TiO$_2$	300 W Xe lamp	None	46.80 $\mu mol \cdot g^{-1} \cdot h^{-1}$	Nessler's reagent	[45]
6%-TiO$_2$	300 W Xe lamp	None	78.9 $\mu mol \cdot g^{-1} \cdot h^{-1}$	Nessler's reagent	[46]
Fe$_{0.1}$Sr$_{0.9}$TiO$_3$	300 W Xe lamp	None	30.1 $\mu mol \cdot g^{-1} \cdot h^{-1}$	Nessler's reagent	[47]
Vo-BiOBr nanosheets	300 W Xe lamp	None	54.70 $\mu mol \cdot g^{-1} \cdot h^{-1}$	Nessler's reagent	[49]
V-g-C$_3$N$_4$[a]	300 W Xe lamp 420 nm > λ	20% CH_3OH	1240 $\mu mol \cdot g^{-1} \cdot h^{-1}$	Nessler's reagent	[50]
Bi$_2$MoO$_6$/Ov-BiOBr	300 W Xe lamp	None	90.7 $\mu mol \cdot g^{-1} \cdot h^{-1}$	Nessler's reagent	[51]
Au/TiO$_2$-Ov	300 W Xe lamp 420 nm > λ	10% CH_3OH	78.6 $\mu mol \cdot g^{-1} \cdot h^{-1}$	Indophenol blue	[52]
Au/(BiO)$_2$CO$_3$	300 W Xe lamp	None	38.2 $\mu mol \cdot g^{-1} \cdot h^{-1}$	Indophenol blue	[53]
BiOCl	500 W Xe lamp	25% CH_3OH	92.4 $\mu mol \cdot g^{-1} \cdot h^{-1}$	Nessler's reagent	[54]
Bi$_5$O$_7$I	300 W Xe lamp	20% CH_3OH	111.5 $\mu mol \cdot L^{-1} \cdot h^{-1}$	Nessler's reagent	[55]
Bi$_5$O$_7$Br	300 W Xe lamp 400 nm > λ	None	1380 $\mu mol \cdot g^{-1} \cdot h^{-1}$	Nessler's reagent	[56]
20Fe-2Al@3DGraphene	500 W Hg lamp	None	430 $\mu mol \cdot g^{-1} \cdot h^{-1}$	Indophenol blue	[57]
Ultrathin MoS$_2$	500 W Xe lamp 420 nm > λ	None	325 $\mu mol \cdot g^{-1} \cdot h^{-1}$	Isotopic labeling	[58]
CuCr-NSs	300 W Xe lamp 400 nm > λ	None	184.8 $\mu mol \cdot L^{-1} \cdot h^{-1}$	Nessler's reagent	[59]
Mo-doped W$_{18}$O$_{49}$	300 W Xe lamp	1 mM Na$_2$SO$_3$	195.5 $\mu mol \cdot g^{-1} \cdot h^{-1}$	Nessler's reagent, Ion chromatography	[60]
BiO quantum dots	500 W Xe lamp	None	1226 $\mu mol \cdot g^{-1} \cdot h^{-1}$	Indophenol blue	[61]
C-WO$_3 \cdot$H$_2$O	500 W Xe lamp	None	205 $\mu mol \cdot g^{-1} \cdot h^{-1}$	Nessler's reagent	[62]
Fe-doped g-C$_3$N$_4$	250 W Na lamp 400 nm < λ < 800 nm	0.1% C_2H_5OH	317.1 $\mu mol \cdot L^{-1} \cdot g^{-1} \cdot h^{-1}$	Nessler's reagent	[63]
5% Ru@n-GaN NWs	300 W Xe lamp	None	120 $\mu mol \cdot g^{-1} \cdot h^{-1}$	Indophenol blue	[64]
Ga$_2$O$_3$-DBD/g-C$_3$N$_4$	500 W Xe lamp	0.04 mM CH_3OH	112.5 $\mu mol \cdot L^{-1} \cdot h^{-1}$	Nessler's reagent	[65]
TiO$_2$@C/g-C$_3$N$_4$	300 W Xe lamp 420 nm > λ	20% CH_3OH	250.6 $\mu mol \cdot g^{-1} \cdot h^{-1}$	Nessler's reagent	[66]
g-C$_3$N$_4$/MgAlFeO	250 W Na lamp 400 nm < λ < 800 nm	0.1% C_2H_5OH	440.4 $\mu mol \cdot L^{-1} \cdot g^{-1} \cdot h^{-1}$	Nessler's reagent	[67]
TiO$_2$/Au/a-TiO$_2$	300 W Xe lamp	None	0.0134 $\mu mol \cdot cm^{-2} \cdot h^{-1}$	Indophenol blue	[68]
Fe$_2$O$_3$	500 W Xe lamp	0.1% C_2H_5OH	1362.5 $\mu mol \cdot L^{-1} \cdot h^{-1}$	Nessler's reagent	[69]
H-Bi$_2$MoO$_6$	300 W Xe lamp with a 420 nm cutoff filter	None	1300 $\mu mol \cdot g^{-1} \cdot h^{-1}$	Nessler's reagent	[70]

[a] Where V denoted nitrogen vacancies

[b] Nessler's reagent, K_2HgI_4, is one of photometric indicators for NH_3 detection and quantification [71]

importance of three-phase interfaces, where a catalyst and two phases reactants such as water and active gas faced, has been demonstrated [77 78]. This indicates that even if highly robust catalysts are prepared, if the supply of N_2 gas and water is insufficient at the region close to the catalyst, the NH_3 production is limited. Thus, environmental engineering, for example, via hydrophobicity control on the catalysts, will be significantly effective. The mechanism, experimental methods, discussion, insights, and suggestions contained in this review provide a good fundamental and foundation for further improvement of photocatalytic NH_3 production.

Choe *et al. Nano Convergence*   (2021) 8:22

Page 11 of 12

Availability of data and materials
The datasets used and analysed during the current study are available from the corresponding references listed.

Declarations

Competing interests
The authors declare that they have no competing interests.

References

1. J.W. Erisman, M.A. Sutton, J. Galloway, Z. Klimont, W. Winiwarter, How a century of ammonia synthesis changed the world. Nat. Geosci. **1**(10), 636 (2008)
2. V. Smil, Detonator of the population explosion. Nature **400**(6743), 415 (1999)
3. J.G. Chen, R.M. Crooks, L.C. Seefeldt et al., Beyond fossil fuel-driven nitrogen transformations. Science **360**(6391), eaar6611 (2018)
4. Y.J. Jang, K.S. Choi, Enabling electrochemical N_2 reduction to NH_3 in the low overpotential region using non-noble metal Bi electrodes via surface composition modification. J Mater Chem A **8**(27), 13842 (2020)
5. D.R. MacFarlane, P.V. Cherepanov, J. Choi, B.H.R. Suryanto, R.Y. Hodgetts, J.M. Bakker, F.M.F. Vallana, A.N. Simonov, A roadmap to the ammonia economy. Joule **4**(6), 1186 (2020)
6. J. John, D.K. Lee, U. Sim, Photocatalytic and electrocatalytic approaches towards atmospheric nitrogen reduction to ammonia under ambient conditions. Nano Converg. **6**(1), 15 (2019)
7. K. Ithisuphalap, H. Zhang, L. Guo, Q. Yang, H. Yang, G. Wu, Photocatalysis and photoelectrocatalysis methods of nitrogen reduction for sustainable ammonia synthesis. Small Methods **3**(6), 1800352 (2019)
8. Y.J. Jang, A.E. Lindberg, M.A. Lumley, K.S. Choi, Photoelectrochemical nitrogen reduction to ammonia on cupric and cuprous oxide photocathodes. ACS Energy Lett. **5**(6), 1834 (2020)
9. G.N. Schrauzer, T.D. Guth, Photolysis of water and photoreduction of nitrogen on titanium dioxide. J Am Chem. Soc. **99**(22), 7189 (1977)
10. G. Zhang, X. Yang, C. He, P. Zhang, H. Mi, Constructing a tunable defect structure in TiO_2 for photocatalytic nitrogen fixation. J. Mater. Chem. A **8**(1), 334 (2020)
11. E. Endoh, J.K. Leland, A.J. Bard, Heterogeneous photoreduction of nitrogen to ammonia on tungsten oxide. J. Phys. Chem **90**(23), 6223 (1986)
12. Q.S. Li, K. Domen, S. Naito, T. Onishi, K. Tamaru, Photocatalytic synthesis and photodecomposition of ammonia over $SrTiO_3$ and $BaTiO_3$ based catalysts. Chem. Lett. **12**(3), 321 (1983)
13. Y. Zhao, S. Zhou, J. Zhao, Y. Du, S.X. Dou, Control of photocarrier separation and recombination at bismuth oxyhalide interface for nitrogen fixation. J. Phys. Chem. Lett. **11**(21), 9304 (2020)
14. L. Yu, Z. Mo, X. Zhu, J. Deng, F. Xu, Y. Song, Y. She, H. Li, and H. Xu, Construction of 2D/2D Z-scheme $MnO_{2-x}/g-C_3N_4$ photocatalyst for efficient nitrogen fixation to ammonia, Green Energy Environ., (2020)
15. H. Gal, G. Alan, F. Frank A. et al., The potential economic feasibility of direct electrochemical nitrogen reduction as a route to ammonia, ChemRxiv, (2019)
16. M. Pourbaix, *Atlas of electrochemical equilibria in aqueous solutions* (National Association of Corrosion Engineers, Houston, Tex., 1974).
17. L. Zhang, H.H. Mohamed, R. Dillert, D. Bahnemann, Kinetics and mechanisms of charge transfer processes in photocatalytic systems: a review. J. Photochem. Photobiol. C-Photochem. Rev. **13**(4), 263 (2012)
18. M.A. Lumley, A. Radmilovic, Y.J. Jang, A.E. Lindberg, K.S. Choi, Perspectives on the development of oxide-based photocathodes for solar fuel production. J. Am. Chem. Soc. **141**(46), 18358 (2019)
19. W. Zhao, J. Zhang, X. Zhu, M. Zhang, J. Tang, M. Tan, Y. Wang, Enhanced nitrogen photofixation on Fe-doped TiO_2 with highly exposed (101)

facets in the presence of ethanol as scavenger. Appl. Catal. B-Environ. **144**, 468 (2014)
20. S. Liu, Y. Wang, S. Wang et al., Photocatalytic fixation of nitrogen to ammonia by single Ru atom decorated TiO_2 nanosheets. ACS Sustain. Chem. Eng. **7**(7), 6813 (2019)
21. Z. Yan, H.W. Wu, A. Han, X. Yu, P. Du, Noble metal-free cobalt oxide (CoO_x) nanoparticles loaded on titanium dioxide/cadmium sulfide composite for enhanced photocatalytic hydrogen production from water. Int. J. Hydrog. Energy **39**(25), 13353 (2014)
22. X. Yue, S. Yi, R. Wang, Z. Zhang, S. Qiu, Cobalt phosphide modified titanium oxide nanophotocatalysts with significantly enhanced photocatalytic hydrogen evolution from water splitting. Small **13**(14), 1603301 (2017)
23. S. Chen, D. Liu, T. Peng, Fundamentals and recent progress of photocatalytic nitrogen-fixation reaction over semiconductors. Sol. RRL **5**(2), 2000487 (2021)
24. S. Zhang, Y. Zhao, R. Shi, G.I.N. Waterhouse, T. Zhang, Photocatalytic ammonia synthesis: recent progress and future. EnergyChem **1**(2), 100013 (2019)
25. P. Chen, N. Zhang, S. Wang et al., Interfacial engineering of cobalt sulfide/graphene hybrids for highly efficient ammonia electrosynthesis. Proc. Natl. Acad. Sci. U. S. A.**116**(14), 6635 (2019)
26. Y. Zhao, R. Shi, X. Bian et al., Ammonia detection methods in photocatalytic and electrocatalytic experiments: how to improve the reliability of NH_3 production rates? Adv. Sci. **6**(8), 1802109 (2019)
27. M. Cong, X. Chen, K. Xia, X. Ding, L. Zhang, Y. Jin, Y. Gao, L. Zhang, Selective nitrogen reduction to ammonia on iron porphyrin-based single-site metal–organic frameworks. J. Mater. Chem. A **9**(8), 4673 (2021)
28. S.Z. Andersen, V. Čolić, S. Yang et al., A rigorous electrochemical ammonia synthesis protocol with quantitative isotope measurements. Nature **570**(7762), 504 (2019)
29. L. Li, C. Tang, D. Yao, Y. Zheng, S.Z. Qiao, Electrochemical nitrogen reduction: identification and elimination of contamination in electrolyte. ACS Energy Lett. **4**(9), 2111 (2019)
30. A.C. Nielander, J.M. McEnaney, J.A. Schwalbe et al., A versatile method for ammonia detection in a range of relevant electrolytes via direct nuclear magnetic resonance techniques. ACS Catal. 9(7), 5797 (2019)
31. F. Wu, Y. Yu, H. Yang et al., Simultaneous enhancement of charge separation and hole transportation in a TiO_2–$SrTiO_3$ core–shell nanowire photoelectrochemical system. Adv. Mater. **29**(28), 1701432 (2017)
32. B. Huang, Y. Liu, Q. Pang, X. Zhang, H. Wang, P.K. Shen, Boosting the photocatalytic activity of mesoporous $SrTiO_3$ for nitrogen fixation through multiple defects and strain engineering. J. Mater. Chem. A **8**(42), 22251 (2020)
33. Z. Ying, S. Chen, S. Zhang, T. Peng, R. Li, Efficiently enhanced N_2 photofixation performance of sea-urchin-like $W_{18}O_{49}$ microspheres with Mn-doping. Appl. Catal. B-Environ. **254**, 351 (2019)
34. P. Huang, W. Liu, Z. He et al., Single atom accelerates ammonia photosynthesis. Sci. China-Chem. **61**(9), 1187 (2018)
35. S. Hu, X. Chen, Q. Li, Y. Zhao, W. Mao, Effect of sulfur vacancies on the nitrogen photofixation performance of ternary metal sulfide photocatalysts. Catal. Sci. Technol. **6**(15), 5884 (2016)
36. D.S. Bhachu, S.J.A. Moniz, S. Sathasivam et al., Bismuth oxyhalides: synthesis, structure and photoelectrochemical activity. Chem. Sci. **7**(8), 4832 (2016)
37. J. Li, H. Li, G. Zhan, L. Zhang, Solar water splitting and nitrogen fixation with layered bismuth oxyhalides. Accounts Chem. Res. **50**(1), 112 (2017)
38. W.L. Huang, Electronic structures and optical properties of BiOX (X = F, Cl, Br, I) via DFT calculations. J. Comput. Chem. **30**(12), 1882 (2009)
39. S. Liu, S. Wang, Y. Jiang, Z. Zhao, G. Jiang, Z. Sun, Synthesis of Fe_2O_3 loaded porous $g-C_3N_4$ photocatalyst for photocatalytic reduction of dinitrogen to ammonia. Chem. Eng. J. **373**, 572 (2019)
40. R. Liu, Z. Chen, Y. Yao, Y. Li, W.A. Cheema, D. Wang, S. Zhu, Recent advancements in $g-C_3N_4$-based photocatalysts for photocatalytic CO_2 reduction: a mini review. RSC Adv. **10**(49), 29408 (2020)
41. R. Shi, Y. Zhao, G.I.N. Waterhouse, S. Zhang, T. Zhang, Defect engineering in photocatalytic nitrogen fixation. ACS Catal. **9**(11), 9739 (2019)
42. Y.J. Jang, M.D. Bhatt, J. Lee, S.H. Choi, B.J. Lee, J.S. Lee, Metal-free artificial photosynthesis of carbon monoxide using N-doped ZnTe nanorod photocathode decorated with N-doped carbon electrocatalyst layer. Adv. Energy Mater. **8**(20), 1702636 (2018)

Choe *et al. Nano Convergence*   (2021) 8:22

Page 12 of 12

43. J.H. Kim, Y.J. Jang, S.H. Choi, B.J. Lee, J.H. Kim, Y.B. Park, C.M. Nam, H.G. Kim, J.S. Lee, A multitude of modifications strategy of $ZnFe_2O_4$ nanorod photoanodes for enhanced photoelectrochemical water splitting activity. J. Mater. Chem. A **6**(26), 12693 (2018)

44. Y.J. Jang, Y.B. Park, H.E. Kim, Y.H. Choi, S.H. Choi, J.S. Lee, Oxygen-intercalated $CuFeO_2$ photocathode fabricated by hybrid microwave annealing for efficient solar hydrogen production. Chem. Mat. **28**(17), 6054 (2016)

45. J. Li, D. Wang, R. Guan, Y. Zhang, Z. Zhao, H. Zhai, Z. Sun, Vacancy-enabled mesoporous TiO_2 modulated by nickel doping with enhanced photocatalytic nitrogen fixation performance. ACS Sustain. Chem. Eng. **8**(49), 18258 (2020)

46. Y. Zhao, Y. Zhao, R. Shi, B. Wang, G.I.N. Waterhouse, L.Z. Wu, C.H. Tung, T. Zhang, Tuning oxygen vacancies in ultrathin TiO_2 nanosheets to boost photocatalytic nitrogen fixation up to 700 nm. Adv. Mater. **31**(16), 1806482 (2019)

47. Z. Ying, S. Chen, T. Peng, R. Li, J. Zhang, Fabrication of an Fe-doped $SrTiO_3$ photocatalyst with enhanced dinitrogen photofixation performance. Eur. J. Inorg. Chem. **2019**(16), 2182 (2019)

48. M. Li, H. Huang, J. Low, C. Gao, R. Long, Y. Xiong, Recent progress on electrocatalyst and photocatalyst design for nitrogen reduction. Small Methods **3**(6), 1800388 (2019)

49. X. Xue, R. Chen, H. Chen et al., Oxygen vacancy engineering promoted photocatalytic ammonia synthesis on ultrathin two-dimensional bismuth oxybromide nanosheets. Nano Lett. **18**(11), 7372 (2018)

50. G. Dong, W. Ho, C. Wang, Selective photocatalytic N_2 fixation dependent on $g-C_3N_4$ induced by nitrogen vacancies. J. Mater. Chem. A **3**(46), 23435 (2015)

51. X. Xue, R. Chen, C. Yan, Y. Hu, W. Zhang, S. Yang, L. Ma, G. Zhu, Z. Jin, Efficient photocatalytic nitrogen fixation under ambient conditions enabled by the heterojunctions of n-type Bi_2MoO_6 and oxygen-vacancy-rich p-type BiOBr. Nanoscale **11**(21), 10439 (2019)

52. J. Yang, Y. Guo, R. Jiang, F. Qin, H. Zhang, W. Lu, J. Wang, J.C. Yu, High-efficiency "working-in-tandem" nitrogen photofixation achieved by assembling plasmonic gold nanocrystals on ultrathin titania nanosheets. J. Am. Chem. Soc. **140**(27), 8497 (2018)

53. C. Xiao, H. Hu, X. Zhang, D.R. MacFarlane, Nanostructured gold/bismutite hybrid heterocatalysts for plasmon-enhanced photosynthesis of ammonia. ACS Sustain. Chem. Eng. **5**(11), 10858 (2017)

54. H. Li, J. Shang, J. Shi, K. Zhao, L. Zhang, Facet-dependent solar ammonia synthesis of BiOCl nanosheets via a proton-assisted electron transfer pathway. Nanoscale **8**(4), 1986 (2016)

55. Y. Bai, L. Ye, T. Chen, L. Wang, X. Shi, X. Zhang, D. Chen, Facet-dependent photocatalytic N_2 fixation of bismuth-rich Bi_5O_7I nanosheets. ACS Appl. Mater. Interfaces **8**(41), 27661 (2016)

56. S. Wang, X. Hai, X. Ding, K. Chang, Y. Xiang, X. Meng, Z. Yang, H. Chen, J. Ye, Light-switchable oxygen vacancies in ultrafine Bi5O7Br nanotubes for boosting solar-driven nitrogen fixation in pure water. Adv. Mater. **29**(31), 1701774 (2017)

57. Y. Yang, T. Zhang, Z. Ge, Y. Lu, H. Chang, P. Xiao, R. Zhao, Y. Ma, Y. Chen, Highly enhanced stability and efficiency for atmospheric ammonia photocatalysis by hot electrons from a graphene composite catalyst with Al_2O_3. Carbon **124**, 72 (2017)

58. S. Sun, X. Li, W. Wang, L. Zhang, X. Sun, Photocatalytic robust solar energy reduction of dinitrogen to ammonia on ultrathin MoS_2. Appl. Catal. B-Environ. **200**, 323 (2017)

59. Y. Zhao, Y. Zhao, G.I.N. Waterhouse et al., Layered-double-hydroxide nanosheets as efficient visible-light-driven photocatalysts for dinitrogen fixation. Adv. Mater. **29**(42), 1703828 (2017)

60. N. Zhang, A. Jalil, D. Wu et al., Refining defect states in $W_{18}O_{49}$ by Mo doping: A strategy for tuning N_2 activation towards solar-driven nitrogen fixation. J. Am. Chem. Soc. **140**(30), 9434 (2018)

61. S. Sun, Q. An, W. Wang, L. Zhang, J. Liu, W.A.G. Iii, Efficient photocatalytic reduction of dinitrogen to ammonia on bismuth monoxide quantum dots. J. Mater. Chem. A **5**(1), 201 (2017)

62. X. Li, W. Wang, D. Jiang, S. Sun, L. Zhang, X. Sun, Efficient solar-driven nitrogen fixation over carbon–tungstic-acid hybrids. Chem. Eur. J. **22**(39), 13819 (2016)

63. S. Hu, X. Chen, Q. Li, F. Li, Z. Fan, H. Wang, Y. Wang, B. Zheng, G. Wu, Fe^{3+} doping promoted N_2 photofixation ability of honeycombed graphitic carbon nitride: the experimental and density functional theory simulation analysis. Appl. Catal. B-Environ. **201**, 58 (2017)

64. L. Li, Y. Wang, S. Vanka, X. Mu, Z. Mi, C.J. Li, Nitrogen photofixation over III-nitride nanowires assisted by ruthenium clusters of low atomicity. Angew. Chem. Int. Ed. **56**(30), 8701 (2017)

65. S. Cao, N. Zhou, F. Gao, H. Chen, F. Jiang, All-solid-state Z-scheme 3,4-dihydroxybenzaldehyde-functionalized Ga_2O_3/graphitic carbon nitride photocatalyst with aromatic rings as electron mediators for visible-light photocatalytic nitrogen fixation. Appl. Catal. B-Environ. **218**, 600 (2017)

66. Q. Liu, L. Ai, J. Jiang, MXene-derived TiO_2@C/g-C_3N_4 heterojunctions for highly efficient nitrogen photofixation. J. Mater. Chem. A **6**(9), 4102 (2018)

67. Y. Wang, W. Wei, M. Li, S. Hu, J. Zhang, R. Feng, In situ construction of Z-scheme g-C3N4/Mg1.1Al0.3Fe0.2O1.7 nanorod heterostructures with high N_2 photofixation ability under visible light. RSC Adv. **7**(29), 18099 (2017)

68. C. Li, T. Wang, Z.J. Zhao, W. Yang, J.F. Li, A. Li, Z. Yang, G.A. Ozin, J. Gong, Promoted fixation of molecular nitrogen with surface oxygen vacancies on plasmon-enhanced TiO_2 photoelectrodes. Angew. Chem. Int. Ed. **57**(19), 5278 (2018)

69. M. Lashgari, P. Zeinalkhani, Photocatalytic N2 conversion to ammonia using efficient nanostructured solar-energy-materials in aqueous media: a novel hydrogenation strategy and basic understanding of the phenomenon. Appl. Catal. A-Gen. **529**, 91 (2017)

70. Y. Hao, X. Dong, S. Zhai, H. Ma, X. Wang, X. Zhang, Hydrogenated bismuth molybdate nanoframe for efficient sunlight-driven nitrogen fixation from air. Chem. Eng. J. **22**(52), 18722 (2016)

71. L. Zhou, C.E. Boyd, Comparison of Nessler, phenate, salicylate and ion selective electrode procedures for determination of total ammonia nitrogen in aquaculture. Aquaculture **450**, 187 (2016)

72. Y. Lin, H. Hu, Y.H. Hu, Role of ZnO morphology in its reduction and photocatalysis. Appl. Surf. Sci. **502**, 144202 (2020)

73. D.Y. Kim, T. Yoon, Y.J. Jang, J.H. Lee, Y. Na, B.J. Lee, J.S. Lee, K.S. Kim, Band gap narrowing of zinc orthogermanate by dimensional and defect modification. J. Phys. Chem. C **123**(23), 14573 (2019)

74. Y.J. Jang, I. Jeong, J. Lee, J. Lee, M.J. Ko, J.S. Lee, Unbiased sunlight-driven artificial photosynthesis of carbon monoxide from CO_2 using a ZnTe-based photocathode and a perovskite solar cell in tandem. ACS Nano **10**(7), 6980 (2016)

75. Y.J. Jang, J. Ryu, D. Hong, S. Park, J.S. Lee, A multi-stacked hyperporous silicon flake for highly active solar hydrogen production. Chem. Commun. **52**(67), 10221 (2016)

76. J. Ryu, Y.J. Jang, S. Choi, H.J. Kang, H. Park, J.S. Lee, S. Park, All-in-one synthesis of mesoporous silicon nanosheets from natural clay and their applicability to hydrogen evolution. NPG Asia Mater. **8**(e248), 1 (2016)

77. N.C. Kani, A. Prajapati, B.A. Collins, J.D. Goodpaster, M.R. Singh, Competing effects of pH, cation identity, H_2O saturation, and N_2 concentration on the activity and selectivity of electrochemical reduction of N_2 to NH_3 on electrodeposited Cu at ambient conditions. ACS Catal. **10**(24), 14592 (2020)

78. X. Wei, M. Pu, Y. Jin, M. Wessling, Efficient electrocatalytic N_2 reduction on three-phase interface coupled in a three-compartment flow reactor for the ambient NH_3 synthesis. ACS Appl. Mater. Interfaces **13**(18), 21411 (2021)

Publisher's Note